Research on Chemical Intermediates (2020) 46:15–31
https://doi.org/10.1007/s11164-019-03933-x

One-step synthesis of $Ag_6Si_2O_7$/AgCl heterojunction composite with extraordinary visible-light photocatalytic activity and stability

Jibo Qin[1] · Weihua Cui[1] · Chuanping Feng[1] · Nan Chen[1] · Miao Li[2]

Received: 13 May 2019 / Accepted: 12 July 2019 / Published online: 27 July 2019

Abstract

In this paper, a Z-scheme $Ag_6Si_2O_7$/AgCl heterojunction composite was successfully constructed via a one-step co-precipitation method and investigated as a novel photocatalyst for the first time. The as-prepared samples were thoroughly characterized by the FESEM, HRTEM, XRD, FTIR, DRS and XPS. The photocatalytic properties of the obtained samples were evaluated by monitoring the degradation efficiency of refractory organic pollutants (methyl orange (MO), rhodamine B (RhB) and phenol) and photocurrent intensity under visible-light irradiation. The $Ag_6Si_2O_7$/AgCl photocatalysts showed drastically enhanced photocatalysis performance compared to the $Ag_6Si_2O_7$ and AgCl. In particular, the 1/72 $Ag_6Si_2O_7$/AgCl composite showed the highest photocatalytic activity, exhibiting a nearly complete degradation of 10 mg/L MO and 20 mg/L phenol within only 40 and 180 min, respectively. The enhancement of photocatalytic activity of the $Ag_6Si_2O_7$/AgCl could be mainly attributed to (1) strong visible-light absorption capacity; (2) effective photogenerated charge separation and transfer through the coupled heterojunction interfaces of $Ag_6Si_2O_7$ and AgCl. Moreover, a possible Z-scheme charge transfer mechanism was proposed based on the experimentation and the theoretical calculation. During the photocatalytic reaction, the $Ag_6Si_2O_7$/AgCl photocatalyst exhibited high mineralization ability for organic pollutants, indicating that it had great practical value in the field of water treatment.

Keywords Z-scheme heterojunction · $Ag_6Si_2O_7$/AgCl · Phenol and MO degradation · Stability

✉ Weihua Cui
cuiwh@cugb.edu.cn

✉ Nan Chen
chennan@cugb.edu.cn

[1] School of Water Resources and Environment, MOE Key Laboratory of Groundwater Circulation and Environmental Evolution, China University of Geosciences (Beijing), Beijing 100083, People's Republic of China

[2] School of Environment, Tsinghua University, Beijing 100084, People's Republic of China

Introduction

Since the beginning of the twenty-first century, environmental crisis has become increasingly rigorous with the rapid development of agriculture, industry and animal husbandry [1]. In particular, dye wastewater discharged from textile or printing and dyeing plants usually has the characteristics of deep color, complex composition, strong biological toxicity and high content of refractory organic pollutants [2]. Photocatalysis, as a very novel and promising technology, has great application prospects in solving problems such as water environmental pollution and water resource shortage [3–7]. A variety of photocatalysts such as transition metal oxides (ZnO, NiO, WO_3) [8–10], transition metal composite oxide (V_2O_5/ZnO, CuO/TiO_2) [11, 12] and sulfide (MoS_2, CdS, CoS_2) [13, 14] have been studied by amounts of researchers to attain their high-efficiency photocatalytic activity for organic contaminants. However, limited light absorption regions of these semiconductors often result in the low light utilization efficiency and low photocatalytic activity [15]. Therefore, it is necessary to explore environmental friendly photocatalysts with visible-light responses and narrow band gap structures to help absorb more sunlight and achieve enhanced photocatalytic properties.

Most recently, Ag_2CO_3 [16], Ag_2CrO_4 [17] and AgX (X = Cl, Br and I) [18–20] have been used as efficient photocatalysts for the degradation of organic pollutants. Among these Ag-based compounds, AgCl, as an inexpensive material with high catalytic performance, has been regarded as the most promising photocatalyst today [21]. AgCl semiconductor can rapidly generate electron–hole pairs under light irradiation, and subsequently, the photogenerated electron can reduce Ag^+ ion to form a metallic silver nanoparticles (NPs) [22]. Previous studies have shown that Ag NP generated on the surface of photocatalyst can cause surface plasmon resonance (SPR) effect under light illumination [23]. This phenomenon will effectively prevent the recombination of photogenerated electron–hole pairs and greatly broaden the light absorption range, which are very advantageous for improving photocatalytic performance. However, AgCl can be reduced to Ag^0, and then, the Ag^0 will soon be oxidized to Ag_2O under illumination, thus improving the catalytic performance of AgCl-based photocatalytic materials [24]. Previous studies showed that seeking a material with good matching with the band structure of AgCl and coupling these two materials to form a heterojunction could effectively avoid the photo-corrosion of Ag/AgCl. For example, it has been reported that Ag/AgCl/TiO_2 [25], Ag/AgCl/ZnO [26], Ag/AgCl/BiOCl [27] and Ag@AgCl/Bi_2WO_6 [28] exhibited superior visible-light photocatalytic activity and stability. It should be noted that these coupling methods had relatively high cost, complicated preparation process and low photocatalytic efficiency for methyl orange (MO). Therefore, further research should be performed to optimize AgCl-based heterostructure photocatalysts.

Silicate compounds are abundant and stable in nature and have been widely used in industry, scientific research and daily life [29]. $Ag_6Si_2O_7$, as a novel photocatalyst, has been used to degrade various contaminants due to its low cost, large specific surface area, narrow band gap, high chemical stability and

environmental friendliness [30, 31]. Meanwhile, the band edges of $Ag_6Si_2O_7$ can match well with those of AgCl. However, to the best of our knowledge, $Ag_6Si_2O_7$/AgCl heterojunction photocatalyst has never been reported in earlier studies. Thus, the development of $Ag_6Si_2O_7$/AgCl heterojunction with a staggered band gap type and high photocatalytic activity is highly anticipated.

Inspired by the above facts, a Z-scheme $Ag_6Si_2O_7$/AgCl heterojunction composite was successfully constructed via a one-step co-precipitation method. Various characterization techniques were used to study the structure, morphology and optical properties of these heterojunctions. Under visible-light irradiation, $Ag_6Si_2O_7$/AgCl heterojunction composite exhibited high catalytic performance and stability for contaminant degradation compared to $Ag_6Si_2O_7$ and AgCl. In addition, the photocatalytic performance and catalyst structure were investigated in detail. Finally, the intermediate products, photodegradation mechanism and the degradation pathways during the reaction process were also demonstrated.

Experimental

Synthesis of $Ag_6Si_2O_7$/AgCl

All the reagents were of analytical grade and used without further purification, and the $Ag_6Si_2O_7$/AgCl composite photocatalyst was prepared by a simple coprecipitate process at room temperature. The accurately weighed 73/24 mM of $AgNO_3$ was dispersed into 40 mL of deionized water. Subsequently, Na_2SiO_3 solution (8.33 mL, 0.005 M) and NaCl solution (60.00 mL, 0.050 M) were simultaneously and slowly added to the $AgNO_3$ mixed solution under continuous magnetic stirring. After that, the obtained samples were separated by centrifugation and washed three times with distilled water and ethanol, respectively. Finally, the photocatalysts were dried in an oven at 65 °C for 24 h. The series of $Ag_6Si_2O_7$/AgCl photocatalysts were prepared by varying the concentration of Na_2SiO_3 solution and denoted x $Ag_6Si_2O_7$/AgCl (x was the molar ratio of Si to Cl). Similarly, pure $Ag_6Si_2O_7$ and AgCl particles were prepared under the same process without the presence of NaCl and Na_2SiO_3 solution, respectively.

Characterization

The morphology of the photocatalysts was carried out by a field emission scanning electron microscopy (FESEM, GeminiSEM500, Zeiss, Germany) and high-resolution transmission electron microscopy (HRTEM, JEM-2100, Jeol, Japan). The crystal property of the samples was carried out using an X-ray diffraction ((XRD, D8 Focus, Bruker, Germany), Cu Kα radiation was used as the radiation source, the tube pressure was 40 kV, the tube flow was 40 mA, $\lambda = 0.15406$ nm, and the scanning range was 10°–80°. Finally, the phase analysis was performed by Search–Match software. The surface functional groups of samples were analyzed by Fourier transform infrared spectroscopy (FTIR, Vertex 70 V, Bruker, Germany). The chemical

composition of the obtained sample was tested using X-ray photoelectron spectroscopy (XPS, ESCALAB 250Xi, Thermo Fisher, USA). The obtained data were subjected to peak-saturation fitting using XPSFEAK software. The UV–Vis diffuse reflection spectra (DRS) were recorded on a UV–visible near-infrared spectrophotometer (Cary 5000, Varian, USA).

Photocatalytic performance

The dye model MO, RhB and highly toxic phenol were selected as the target pollutants for evaluating the catalytic activity of the photocatalyst under visible-light illumination. The light source was supplied by a 300 W Xe lamp (40 mW/cm^2, CEL-HXF300, China) without a UV-cut filter. Meanwhile, the vertical distance between the light source and the reaction solution was kept at 15 cm, with 300 mL of beaker as a reactor. Before the start of the photocatalytic experiment, a total of 0.1 g of photocatalyst ($Ag_6Si_2O_7$, AgCl, $Ag_6Si_2O_7$/AgCl) was uniformly dispersed in 100 mL of MO (10 mg/L), RhB (10 mg/L) aqueous solution and phenol solution (20 mg/L). Subsequently, the suspension was vigorously stirred under dark conditions for 30 min to achieve an adsorption–desorption equilibrium of the photocatalyst and the reaction solution. Finally, the lamp was turned on and the photocatalytic reaction began, 2 mL of reaction solution at regular intervals. The supernatants of reaction solution were analyzed by UV–Vis spectrophotometer (DR6000, HACH, USA) or high-performance liquid chromatography (Agilent 1206, Agilent Technologies, USA). The degradation efficiency (%) was calculated by the following equation:

$$\text{Degradation efficiency } (\%) = \left(C_0 - C_t\right)/C_0 \times 100\% \quad (1)$$

where C_0 (mg/L) and C_t (mg/L) are the concentrations of the target organic solution at irradiation time 0 and t (min), respectively.

Results and discussion

Characterization

FESEM and HRTEM

The surface morphology and size of the obtained $Ag_6Si_2O_7$, AgCl and 1/72 $Ag_6Si_2O_7$/AgCl composite were visualized through TESEM and HRTEM, as depicted in Fig. 1. Clearly, the pristine $Ag_6Si_2O_7$ (Fig. 1a) exhibited smooth spherical structure, and the average size was about 100–150 nm. Meanwhile, there was no obvious agglomeration, indicating that the $Ag_6Si_2O_7$ particles had good dispersibility. As shown in Fig. 1b, the AgCl particles presented a uniform spherical structure with a diameter of about 2–5 μm. As for the $Ag_6Si_2O_7$/AgCl composite (Fig. 1c), it was observed that the size of $Ag_6Si_2O_7$/AgCl particle (ca. 300–500 nm) was increased obviously in comparison with that of the pure $Ag_6Si_2O_7$, which indicated that we successfully and tightly coupled $Ag_6Si_2O_7$ nanospheres with AgCl.

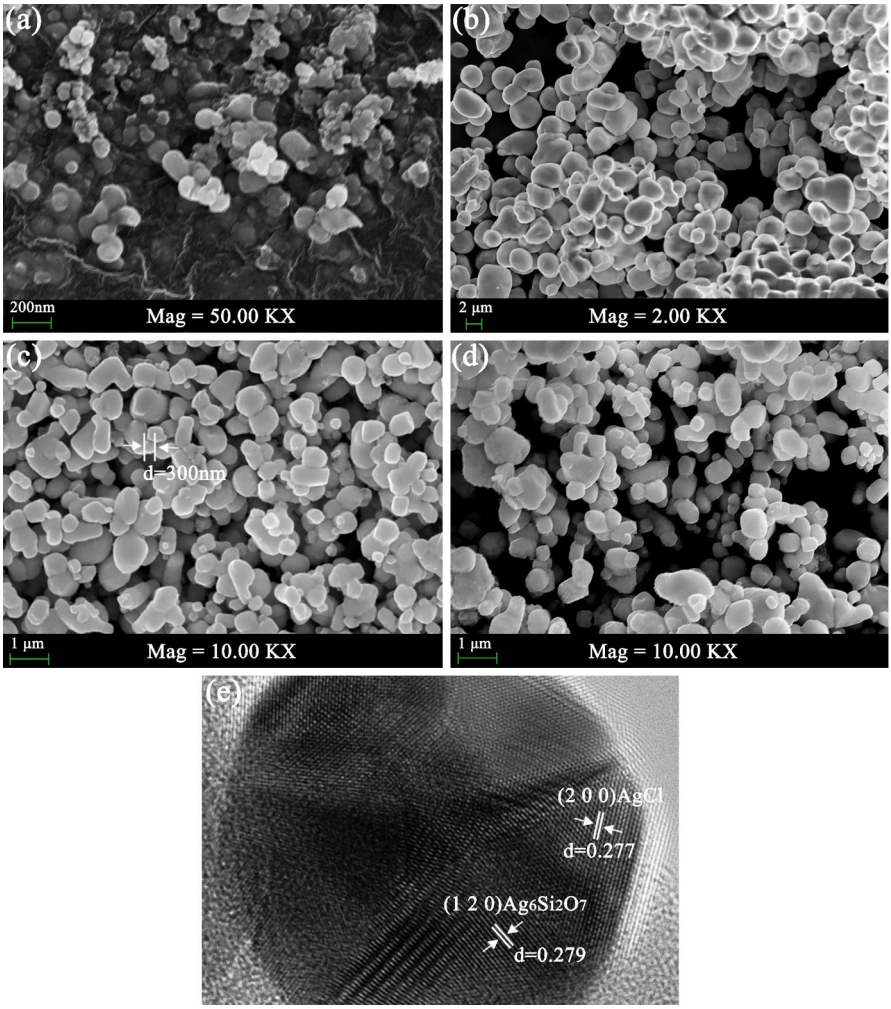

Fig. 1 FESEM images of $Ag_6Si_2O_7$ (**a**); AgCl (**b**); 1/72 $Ag_6Si_2O_7$/AgCl (**c**); recycled 1/72 $Ag_6Si_2O_7$/AgCl (**d**); and HRTEM image 1/72 $Ag_6Si_2O_7$/AgCl (**e**)

In this way, a heterojunction that promoted photogenerated charge separation would be constructed at the interface between $Ag_6Si_2O_7$ and AgCl. Furthermore, the 1/72 $Ag_6Si_2O_7$/AgCl sample after four successful cycles was also examined by the FESEM. As shown in Fig. 1d, regardless of size or morphology, there was no significant difference between recycled and fresh samples, which indicated the $Ag_6Si_2O_7$/AgCl had a good stability and reusability.

In order to further ascertain the as-prepared heterojunction structure, 1/72 $Ag_6Si_2O_7$/AgCl composite was investigated by HRTEM. From the magnified HRTEM image (Fig. 1e), we can more intuitively observe that $Ag_6Si_2O_7$ and AgCl were tightly combined. In addition, Fig. 1e also clearly exhibits the fringes

with the lattice spacing of 0.264 and 0.245 nm, which can be indexed to the (1 2 4) plane of $Ag_6Si_2O_7$ and (0 0 3) plane of AgCl, respectively, well confirming the existence of $Ag_6Si_2O_7$/AgCl heterojunction.

XRD

The crystal properties and phase composition of the synthesized photocatalysts (Ag_6Si_2O, AgCl and $Ag_6Si_2O_7$/AgCl) were characterized by XRD. As shown in Fig. 2a, all the diffraction peaks of pure AgCl powder were in good agreement with cubic phase of AgCl (JCPDS No. 31-1238) [32]; the intense and sharp diffraction peaks indicated that the obtained AgCl catalysts were well crystallized. As for the patterns of the composite, it was difficult to find the characteristic peak of Ag^0 and $Ag_6Si_2O_7$, which can be attributed to the little content of Ag^0 and $Ag_6Si_2O_7$ in the composite sample; therefore, its characteristic peak was completely covered by AgCl. Meanwhile, no impurity peak was found in the

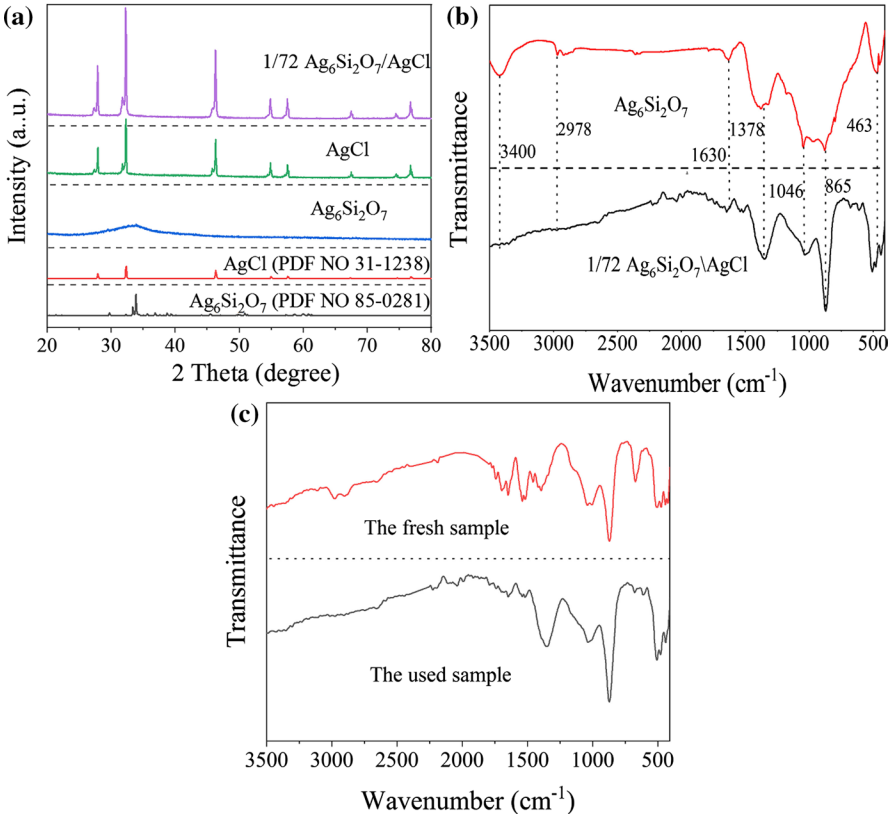

Fig. 2 XRD patterns (**a**) and FTIR spectra (**b**, **c**) of samples

$Ag_6Si_2O_7$/AgCl heterojunction, which suggested that the photocatalyst was only composed of $Ag_6Si_2O_7$ and AgCl.

To further confirm the presence of $Ag_6Si_2O_7$ in composite samples, the synthesized $Ag_6Si_2O_7$ and 1/72 $Ag_6Si_2O_7$/AgCl photocatalysts were characterized by FTIR analysis. As shown in Fig. 2b, the strong absorption peak of $Ag_6Si_2O_7$ and 1/72 $Ag_6Si_2O_7$/AgCl at 3400 cm^{-1} may be associated with the O–H stretching vibration of water molecules on the surface of $Ag_6Si_2O_7$ and $Ag_6Si_2O_7$/AgCl [33]. According to the reports of previous studies, the apparent peaks at 1378 and 1630 cm^{-1} could be attributed to the bending vibration of H_2O [23]; the band at around 463 cm^{-1} was assigned to the stretching vibration of Si–O–Si bond of $Ag_6Si_2O_7$. The sharp peaks in the region of 865 and 1046 cm^{-1} for samples ($Ag_6Si_2O_7$ and 1/72 $Ag_6Si_2O_7$/AgCl) might be assigned to the bending vibration of Si–O [34]. Meanwhile, the peak at about 2978 cm^{-1} corresponded to the C–H bond of ethanol on the surface of the catalyst. In summary, all the peaks of $Ag_6Si_2O_7$ can be observed in the FTIR spectrum of the composite photocatalyst, which further proved the existence of $Ag_6Si_2O_7$ in the composite sample. In addition, Fig. 3d shows that there was no significant

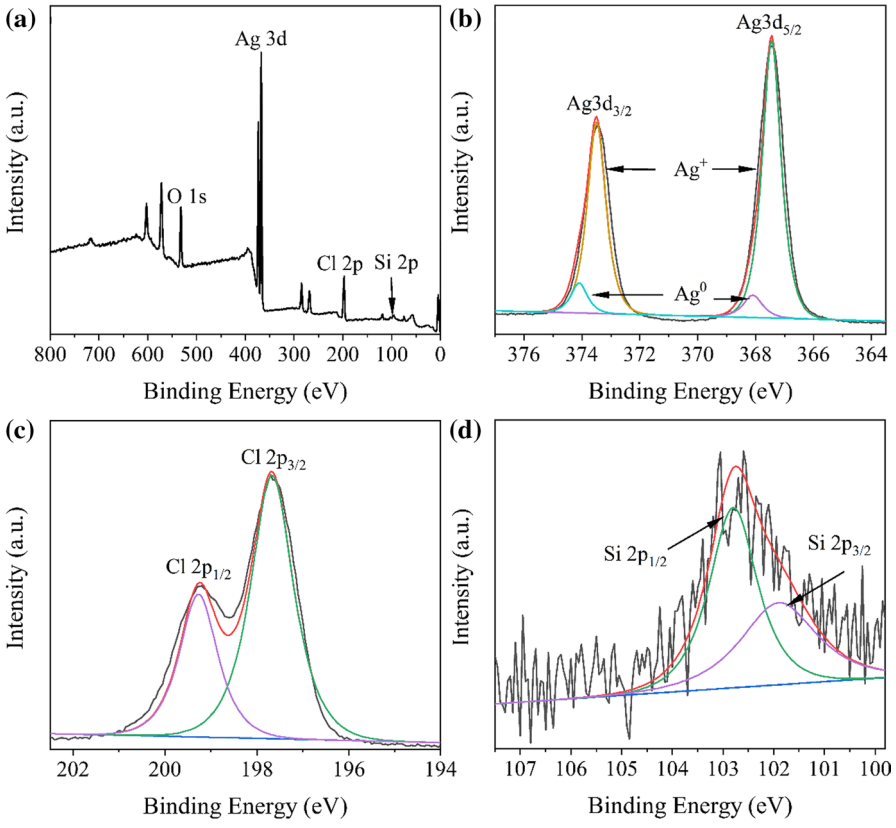

Fig. 3 The XPS spectra of 1/72 $Ag_6Si_2O_7$/AgCl (**a**); Ag 3*d* (**b**); Cl 2*p* (**c**); and Si 2*p* (**d**)

difference in the FTIR spectra between the recycled sample and the fresh sample, which again indicated the $Ag_6Si_2O_7$/AgCl composite has high structural stability.

XPS

The surface composition of the as-prepared samples was further analyzed by XPS analysis. Ag 3*d*, Cl 2*p*, O 1*s* and Si 2*p* transitions were identified in the measured XPS spectrum of 1/72 $Ag_6Si_2O_7$/AgCl (Fig. 3a), revealing that the material was indeed consisted of Ag, Cl, O and Si elements. The spectrum of Ag 3*d* (Fig. 3b) showed that it consists of two individual peaks at the binding energies of 373.42 (Ag 3*d*3/2) and 367.42 eV(Ag 3*d*5/2) [35]. Meanwhile, the above two peaks could be further deconvoluted into different peaks at 373.42/374.15 eV and 367.42/368.05 eV, respectively [15]. We speculated that the characteristic peaks at 374.15 and 368.05 eV might be caused by the presence of metal Ag^0. Through further research, we found that the spin energy separation of these two peaks (374.15 and 368.05 eV) was 6.10 eV, which indicated that Ag^0 was indeed presented in the $Ag_6Si_2O_7$/AgCl composite photocatalyst [36]. Meanwhile, the two peaks at 367.42 and 373.42 eV could be attributed to Ag^+, and the molar ratio of Ag^+ to Ag^0 on the surface of $Ag_6Si_2O_7$/AgCl was quantitatively calculated to be about 9.5:1.0. The existence of Ag^0 may be attributed to the fact that the composite photocatalyst was exposed to sunlight during the preparation process, resulting in Ag^+ accepting photogenerated electrons and generating Ag^0. As shown in Fig. 3c, the sample displayed double peaks located at 199.27 and 197.67 eV. According to the early reports of literature, we can determine the above two peaks to the characteristic of Cl 2*p*1/2 and Cl 2*p*3/2, respectively [37]. Figure 3d reveals that the characteristic peaks at 102.80 and 101.90 eV were ascribed to Si 2*p*1/2 and Si 2*p*3/2 of $Ag_6Si_2O_7$ [30].

DRS

The UV–Vis DRS was adopted to detect the light absorption ability of $Ag_6Si_2O_7$, AgCl and $Ag_6Si_2O_7$/AgCl composite. Obviously, pure AgCl exhibited a strong absorption only in UV-light region owing to its large band gap energy (Fig. 4a). After coupling $Ag_6Si_2O_7$ with AgCl, $Ag_6Si_2O_7$/AgCl showed a strong light absorption within the entire visible region. This phenomenon can be attributed to two reasons: (1) the introduction of photosensitive material $Ag_6Si_2O_7$; (2) the surface plasmon absorption of Ag^0 in composite [37, 38]. The band gap of samples was calculated by the Kubelka–Munk expression [39]:

$$(h\nu\alpha)^{1/n} = A\left(h\nu - E_g\right) \tag{2}$$

where α is the optical absorption coefficient; $h\nu$ is the incident photonic energy (eV); A is the proportionality constant; E_g is the band gap energy (eV); and n is a factor that depends on the kind of optical transition induced by photon absorption (1/2 and 2 for direct and indirect transitions, respectively; here n is 1/2).

Figure 4b displays the E_g value of narrow band gap 1/72 $Ag_6Si_2O_7$/AgCl (0.74 eV) was lower than that of AgCl (3.57 eV) and $Ag_6Si_2O_7$ (1.34 eV), which

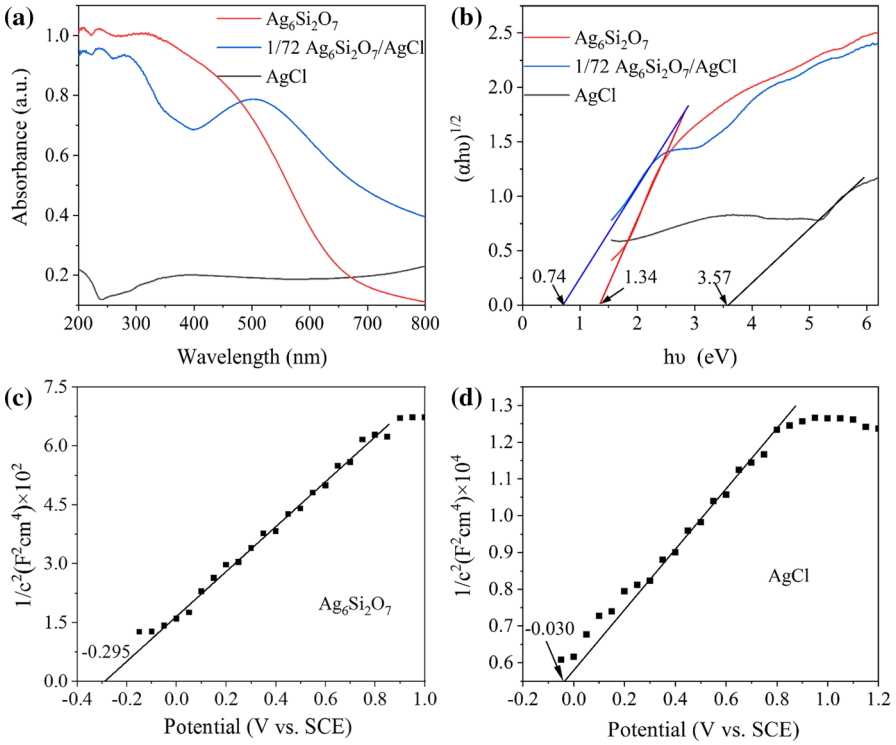

Fig. 4 UV–Vis diffuse reflectance spectra (**a**); band energy (**b**); and Mott–Schottky curve of $Ag_6Si_2O_7$ (**c**) and AgCl (**d**) samples

demonstrated that the combination of $Ag_6Si_2O_7$ with AgCl can effectively capture and utilize more incident light and excite more photogenerated charges to improve the visible-light photocatalytic performance of $Ag_6Si_2O_7$/AgCl. We observed both the light absorption range and the band gap of the composite sample were superior to $Ag_6Si_2O_7$, and speculated that may be due to the presence of Ag^0 in the composite sample.

The band alignment plays a vital role in the process of decomposing organic pollutants by composite photocatalysts [40]. Therefore, a series of Mott–Schottky analyses were used to estimate and calculate the conduction band (CB) and the position of photocatalysts ($Ag_6Si_2O_7$ and AgCl). Figure 4c, d shows that the flat band potentials of $Ag_6Si_2O_7$ and AgCl were − 0.295 and − 0.030 V (vs. SCE), respectively, corresponding to − 0.055 and 0.210 eV (vs. NHE). At the same time, as n-type semiconductors, the CB of $Ag_6Si_2O_7$ and AgCl was 0–0.1 eV higher than their flat potential [41]. Combining the above analysis with the band gap value of photocatalysts, we can conclude the CB/valence band (VB) potential of $Ag_6Si_2O_7$ and AgCl was − 0.05/1.29 and 0.22/3.59 eV, respectively.

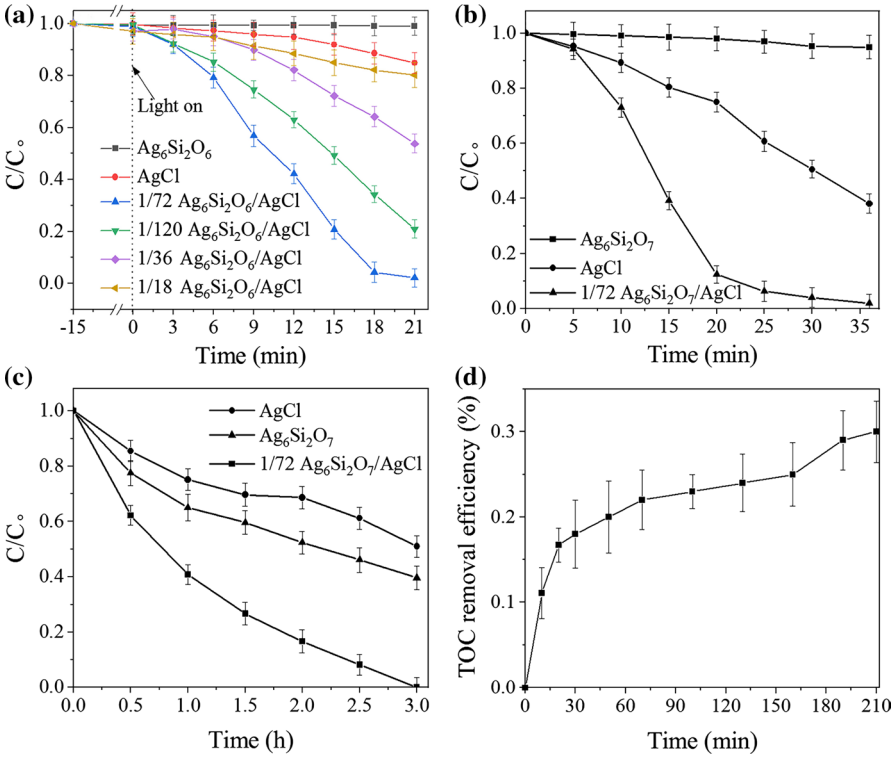

Fig. 5 Photocatalytic activities of the samples toward the MO (**a**) and RhB (**b**) degradation; photodegradation curves of phenol over $Ag_6Si_2O_7$, AgCl and 1/72 $Ag_6Si_2O_7$/AgCl (**c**); TOC removal on the MO solution in the presence of the 1/72 $Ag_6Si_2O_7$/AgCl catalyst (**d**)

Photocatalytic activity

The photocatalytic activity of $Ag_6Si_2O_7$/AgCl composite was investigated by the degradation of MO under visible-light irradiation ($\lambda > 420$ nm). As shown in Fig. 5a, the 1/72 $Ag_6Si_2O_7$/AgCl exhibited the highest photocatalytic activity than other samples, and 98% of MO can be photodegraded within 8 min. However, only 16% of MO can be photodegraded by pure AgCl, which indicated that the introduction of $Ag_6Si_2O_7$ was an effective strategy to promote the photocatalytic performance of AgCl-based composite photocatalysts. Meanwhile, when the content of $Ag_6Si_2O_7$ was insufficient or excessive, it was not conducive to the improvement in the photocatalytic performance of the composite material. Since the content of $Ag_6Si_2O_7$ was insufficient, the heterojunction between $Ag_6Si_2O_7$ and AgCl would not be completely constructed, and much more $Ag_6Si_2O_7$ may mask the active sites of AgCl. It is well known that the adsorption capacity of catalysts for pollutants plays a key role in the photocatalytic process [42–45]. Figure 5a shows that only a small amount of methyl orange was adsorbed on the surface of the composite catalyst during the dark reaction, so the adsorption in

the reaction system contributed little to the performance enhancement of the composite photocatalyst. Figure 5b shows the 1/72 $Ag_6Si_2O_7$/AgCl photocatalyst also had superior catalytic performance for the degradation of RhB, with 98.1% degradation of RhB in 36 min, which was 16 times of $Ag_6Si_2O_7$ and 1.5 times of AgCl. We speculated that the enhancement of the photocatalytic performance of the $Ag_6Si_2O_7$/AgCl composite photocatalyst could be attributed to the following points: (1) The introduction of the photosensitive material $Ag_6Si_2O_7$ broadened the photo-response range of composite photocatalyst; (2) the narrow band gap of the composite enhanced its utilization of incident light and stimulated more photogenerated electrons/hole pairs; (3) the formation of heterojunctions accelerated the separation efficiency of photogenerated charges.

In order to further prove that the $Ag_6Si_2O_7$/AgCl photocatalytic material had excellent photocatalytic performance, wide application range and no selectivity for degraded pollutants, we again evaluated the photocatalytic activity of $Ag_6Si_2O_7$/AgCl by degradation of a highly toxic refractory substance (phenol). As revealed in Fig. 5c, the $Ag_6Si_2O_7$/AgCl heterojunction exhibited much higher photocatalytic efficiency than the pure $Ag_6Si_2O_7$ and AgCl, decomposing 100% of phenol in 3 h. In addition, we also found that the catalytic activity of $Ag_6Si_2O_7$ was better than that of AgCl when degrading phenol, which was different from the degradation experiment of MO. It can be speculated to the presence of selectivity of $Ag_6Si_2O_7$ and AgCl for pollutants (MO, RhB and phenol). Meanwhile, it was worth noting that the catalytic performance of $Ag_6Si_2O_7$ in the degradation of phenol was higher than that of AgCl, but its catalytic activity was not as good as that of AgCl when degrading MO and RhB, which might be attributed to the selectivity of contaminants.

The ultimate goal of organic pollutant treatment in water is to achieve full mineralization. In general, the total organic carbon (TOC) value is usually used to indicate the mineralization of organic matter. Herein, the TOC removal efficiency of MO by 1/72 $Ag_6Si_2O_7$/AgCl was investigated (Fig. 5d). With the extension of irradiation time, the removal efficiency of TOC was gradually increased, and the 1/72 $Ag_6Si_2O_7$/AgCl photocatalytic material can mineralize 30.2% of MO within 3 h, indicating that the material had great practical application potential for the treatment of organic pollutant wastewater.

Photocurrent properties and stability of the $Ag_6Si_2O_7$/AgCl

It is well known that there is a positive correlation between transient photocurrent density and photogenerated charge separation efficiency [46]. In order to further study the mechanism of generation, separation and transfer of photogenerated charges, we tested and analyzed the transient photocurrent density of photocatalytic materials. As shown in Fig. 6a, the photocurrent intensity of the 1/72 $Ag_6Si_2O_7$/AgCl electrode was ca. 22.91 μA/cm^2, while that of AgCl and $Ag_6Si_2O_7$ was as low as 2.10 and 1.21 μA/cm^2, respectively. The significantly enhanced photocurrent of 1/72 $Ag_6Si_2O_7$/AgCl indicated the presence of enhanced interfacial charge separation between AgCl and $Ag_6Si_2O_7$, which was very advantageous for the improvement in its photocatalytic performance.

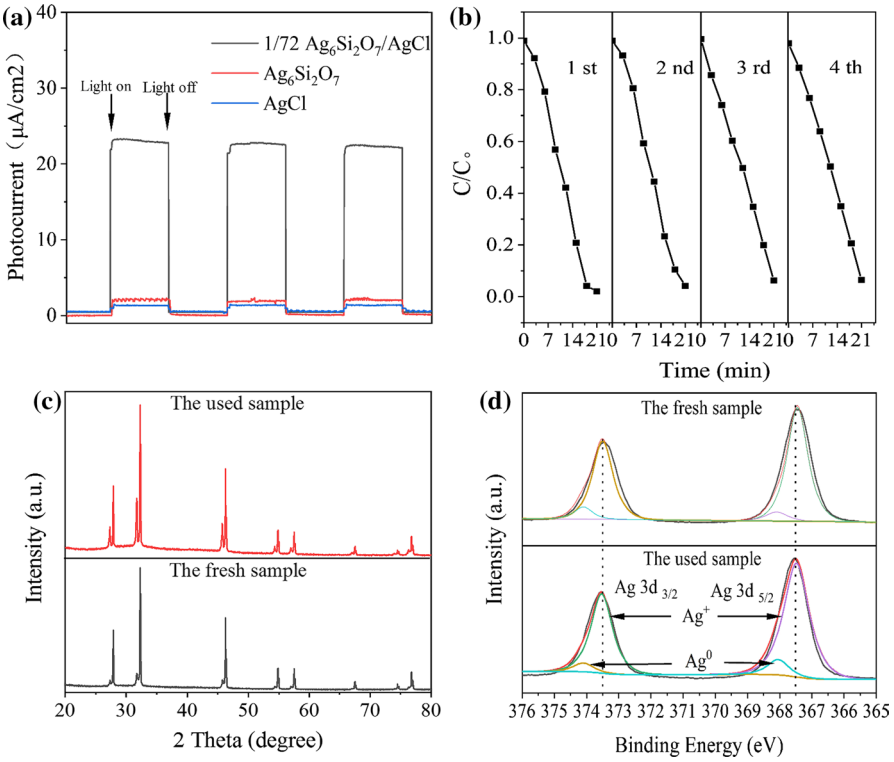

Fig. 6 Transient photocurrent densities of samples (**a**); repeated photocatalytic experiments of the 1/72 $Ag_6Si_2O_7$/AgCl nanocomposite under simulated visible light (catalyst dosage = 1 g/L, C_0 = 10 mg/L) (**b**); XRD patterns (**c**) and XPS spectra (**d**) of 1/72 $Ag_6Si_2O_7$/AgCl before and after cyclic test

The catalytic stability of $Ag_6Si_2O_7$/AgCl was an important parameter to evaluate its practical application value. Therefore, the photocatalytic stability of 1/72 $Ag_6Si_2O_7$/AgCl heterojunction composite was evaluated by multiple successive MO degradation experiments. The results of the recycling test (Fig. 6b) clearly showed that even after four successful cycles, the catalytic activity of the photocatalyst was not significantly deactivated, indicating that the photocatalyst had high practical application potential. Meanwhile, the catalyst stability of $Ag_6Si_2O_7$/AgCl photocatalyst was better than some other $Ag_6Si_2O_7$-based photocatalysis, such as $Ag_6Si_2O_7$/BiOBr [30] and BiOCl/$Ag_6Si_2O_7$ [47].

To further investigate the chemical stability of the obtained photocatalyst, the 1/72 $Ag_6Si_2O_7$/AgCl composite after four successful cycles was collected and further characterized by XRD and XPS. As shown in Fig. 6c, the main XRD peaks of the recycled 1/72 $Ag_6Si_2O_7$/AgCl sample did not change significantly, indicating that its crystal structures were not severely damaged [48]. Furthermore, the XPS spectra of Ag 3*d* in the recycled sample are revealed in Fig. 6d, where the area ratio of Ag^+ to Ag^0 had slightly increased, demonstrating that a small amount of Ag^+ was reduced to Ag^0. This phenomenon indicated that the

$Ag_6Si_2O_7$/AgCl heterostructure was slightly damaged after repeated experiments, which explained why the photocatalytic effect of the material had been slightly decreased after four cycles of testing. Based on the above analysis results of XRD and XPS, we can draw a conclusion that the $Ag_6Si_2O_7$/AgCl composite possessed great application prospects in the field of organic wastewater purification.

Photocatalytic mechanism

In order to understand which active substance played a major role in the degradation of MO by $Ag_6Si_2O_7$/AgCl photocatalyst, *p*-benzoquinone (as superoxide radicals ($\cdot O_2^-$) scavenger), EDTA-2 Na (as holes (h^+) scavenger) and isopropanol (as hydroxyl radicals (·OH) scavenger) were added to the reaction system separately. As shown in Fig. 7a, the addition of IPA had little effect on the catalytic performance of the photocatalyst, demonstrating that ·OH did not exist or was not the main active

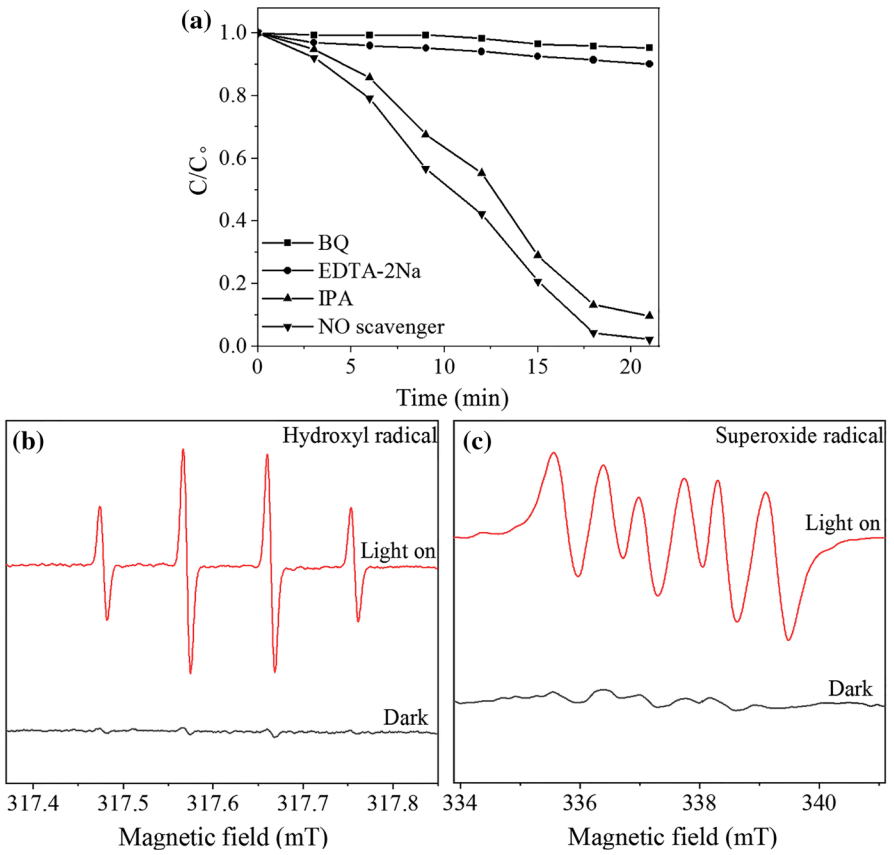

Fig. 7 Reactive species trapping experiments (**a**); ESR spectra of the DMPO—·OH (**b**) and DMPO—$\cdot O_2^-$ (**c**) adducts recorded with 1/72 $Ag_6Si_2O_7$/AgCl under visible-light irradiation

substance for degrading contaminants in the reaction system. However, BQ and EDTA-2 Na caused a significant decrease in the degradation efficiency of pollutants.

In order to further confirm the kind of active substances involved in the photocatalysis process, we carried out the ESR technique using DMPO as a spin trap to capture $\cdot O_2^-$ and ·OH. As shown in Fig. 7b, c, four characteristic peaks belonging to ·OH and six characteristic peaks belonging to $\cdot O_2^-$ can be clearly observed, indicating that there were indeed a small amount of ·OH and a large number of $\cdot O_2^-$ in the photocatalytic process, and $\cdot O_2^-$ dominated the photocatalysis process. Combined with the analysis results of the ESR experiment, it can be found that h^+ and $\cdot O_2^-$ were the mainly active species, while ·OH was not considered to play a key role in the degradation process.

To the best of our knowledge, there were two different interpretations of the mechanism for degrading contaminants in *n–n* composite photocatalysts: (1) traditional heterojunction-type mechanism; (2) Z-scheme mechanism. As shown in Scheme 1, obviously, the mechanism of this experiment did not confirm to the traditional photocatalytic mechanism. Since the CB level of AgCl was less negative than the $O_2/\cdot O_2^-$ (−0.046 eV vs. NHE) [49], it was impossible for the photogenerated electron in the CB of AgCl to reduce the adsorbed O_2 to produce $\cdot O_2^-$ which played a key role in photocatalytic degradation of contaminants.

Based on the above theoretical calculations and experimental results, we concluded that the charge transfer in the $Ag_6Si_2O_7$/AgCl composite photocatalyst might follow the Z-scheme mechanism (Scheme 2). Both $Ag_6Si_2O_7$ and Ag^0 can effectively absorb incident light and rapidly generate a large number of photogenerated electrons and hole pairs under visible-light irradiation. Since the electrons of Ag nanoparticles were more likely to migrate into the CB of $Ag_6Si_2O_7$ and the CB level of $Ag_6Si_2O_7$ was lower than the $O_2/\cdot O_2^-$ potential, the O_2 participating in this reaction can be reduced to $\cdot O_2^-$ by electrons in CB of $Ag_6Si_2O_7$, which was

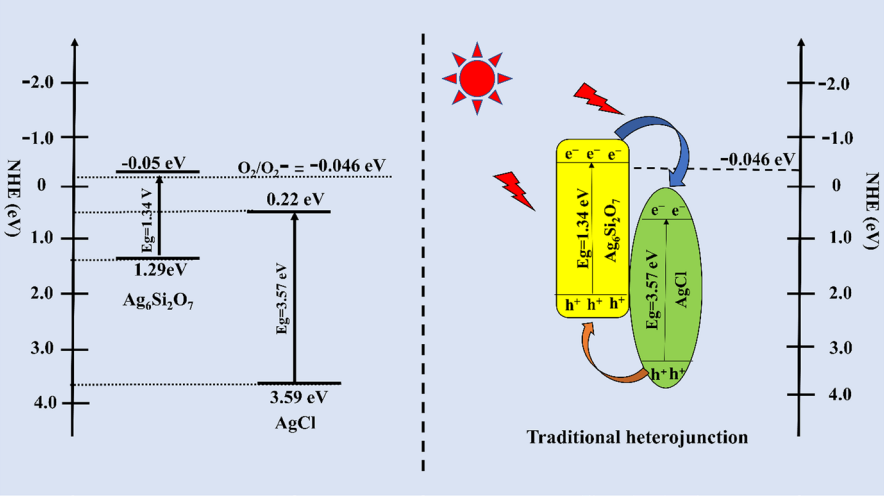

Scheme. 1 Traditional photocatalytic mechanism of the $Ag_6Si_2O_7$/AgCl photocatalyst

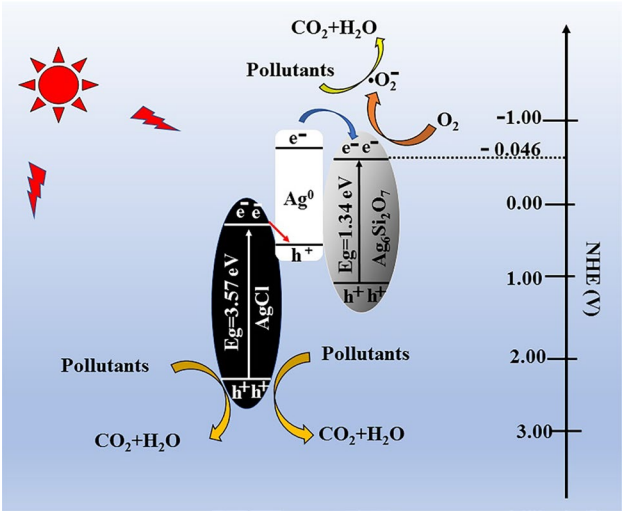

Scheme. 2 Z-scheme photocatalytic mechanism of the $Ag_6Si_2O_7$/AgCl photocatalyst

consistent with the results of the active species capture experiments. For AgCl, the photogenerated electrons in CB might recombine rapidly with the holes of the Ag nanoparticles. This phenomenon can be attributed to the formation of a high Schottky barrier of Ag^0 at the Ag^0/AgCl interface [28], which effectively extended the lifetime of the photogenerated holes with excellent oxidation properties and successfully enhanced the photocatalytic activity. In addition, the holes on the VB of AgCl may directly oxidize dye molecules or oxidize water molecules to form a small amount of ·OH active species ($(\cdot OH/H_2O) = 1.99$ eV vs. NHE)) [50].

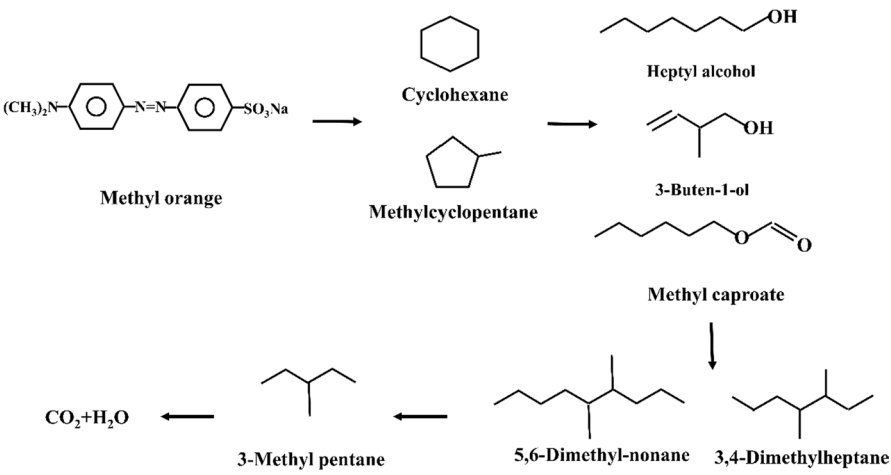

Fig. 8 Degradation pathway proposed on the basis of GC/MS analysis during photodegradation of MO

Degradation pathway

In this study, GC–MS analysis was carried out to identify the intermediate process of MO in the photocatalytic reaction process. Based on the above analysis, we proposed a specific degradation pathway (Fig. 8). In the initial stage of the catalytic reaction, we detected methyl cyclopentane with retention time (RT) 2.193 min and cyclohexane with RT 2.421 min. It can be concluded that these two substances might be caused by the break of the azo group of MO, with the extension of irradiation time, heptyl alcohol with RT 2.593 min, 3-buten-1-ol with RT 2.049 min and methyl caproate with RT 2.147 min. Eventually, the above substances were degraded into small molecular alkanes and then converted into H_2O and CO_2.

Conclusions

In summary, a novel Z-scheme $Ag_6Si_2O_7$/AgCl composite was successfully constructed via a one-step co-precipitation method at room temperature. The obtained photocatalytic samples were fully characterized by FESEM, TEM, HRTEM, XRD, FTIR, DRS and XPS techniques. As a novel, high-efficiency and narrow band gap photocatalyst, $Ag_6Si_2O_7$/AgCl exhibited a high catalytic activity for degradation of various organic pollutants (MO, RhB and phenol), which can be attributed to the Z-scheme photogenerated charge transfer mechanism, thus enhancing the redox ability of composite photocatalytic materials. Meanwhile, the super-catalytic stability of the $Ag_6Si_2O_7$/AgCl photocatalyst indicated that it might have great application prospects in the field of practical organic wastewater treatment. In addition, based on the analysis results of the active substance capture experiments, two possible photocatalytic mechanisms were proposed and discussed in detail. It was noteworthy that this was the first report regarding the photocatalytic decomposition of organic compounds by using $Ag_6Si_2O_7$/AgCl composites.

Acknowledgements The authors acknowledge financial support from the National Natural Science Foundation of China (NSFC) (No. 21876159) and the Fundamental Research Funds for the Central Universities (No. 2652018181).

References

1. H. Guo, C.G. Niu, X.J. Wen, L. Zhang, C. Liang, X.G. Zhang, D.L. Guan, N. Tang, G.M. Zeng, J. Colloid Interface Sci. **513**, 852 (2017)
2. Z. Men, P. Wang, Q. Cao, Shandong Chem. Ind. **46**, 169 (2017)
3. N. Mohaghegh, E. Rahimi, M.R. Gholami, Mater. Sci. Semicond. Process. **39**, 506 (2015)
4. A. Sudhaik, P. Raizada, P. Shandilya, D.-Y. Jeong, J.-H. Lim, P. Singh, J. Ind. Eng. Chem. **67**, 28 (2018)
5. A. Sudhaik, P. Raizada, P. Shandilya, P. Singh, J. Environ. Chem. Eng. **6**, 3874 (2018)
6. P. Singh, P. Shandilya, P. Raizada, A. Sudhaik, A. Rahmani-Sani, A. Hosseini-Bandegharaei, Arab. J. Chem. (2018). https://doi.org/10.1016/j.arabjc.2018.12.001
7. V. Hasija, P. Raizada, A. Sudhaik, K. Sharma, A. Kumar, P. Singh, S.B. Jonnalagadda, V.K. Thakur, Appl. Mater. Today **15**, 494 (2019)
8. J. Kim, C.W. Lee, W. Choi, Environ. Sci. Technol. **44**, 6849 (2010)
9. Y. Wang, D. Li, Q. Ma, J. Tian, Y. Song, X. Xi, X. Dong, W. Yu, J. Wang, G. Liu, RSC Adv. **8**, 11051 (2018)

10. M.A. Hernández-Carrillo, R. Torres-Ricárdez, M.F. García-Mendoza, E. Ramírez-Morales, L. Rojas-Blanco, L.L. Díaz-Flores, G.E. Sepúlveda-Palacios, F. Paraguay-Delgado, G. Pérez-Hernández, Catal. Today (2018). https://doi.org/10.1016/j.cattod.2018.04.060
11. H. Yin, K. Yu, C. Song, R. Huang, Z. Zhu, ACS Appl. Mater. Interfaces **6**, 14851 (2014)
12. Y. Li, Z. Hu, S. Liu, X. Duan, B. Wang, React. Kinet. Mech. Catal. **112**, 559 (2014)
13. B. Ma, Y. Wang, X. Tong, X. Guo, Z. Zheng, X. Guo, Catal. Sci. Technol. **7**, 2805 (2017)
14. X. Zong, G. Wu, H. Yan, G. Ma, J. Shi, F. Wen, L. Wang, C. Li, J. Phys. Chem. C **114**, 1963 (2010)
15. L. Ai, C. Zhang, J. Jiang, Appl. Catal. B Environ. **s142–143**, 744 (2013)
16. G. Dai, J. Yu, G. Liu, J. Phys. Chem. C **116**, 15519 (2012)
17. Y. Liu, H. Yu, M. Cai, J. Sun, Catal. Commun. **26**, 63 (2012)
18. H. Tang, Y. Wang, D. Zhang, K. Wu, H. Huang, J. Mater. Sci. Mater. Electron. **27**, 6955 (2016)
19. Z. Chen, W. Wang, Z. Zhang, X. Fang, J. Phys. Chem. C **117**, 19346 (2013)
20. D. Chen, T. Li, Q. Chen, J. Gao, B. Fan, J. Li, X. Li, R. Zhang, J. Sun, L. Gao, Nanoscale **4**, 5431 (2012)
21. J. Guo, H. Shi, X. Huang, H. Shi, Z. An, J. Colloid Interface Sci. **515**, 10 (2018)
22. Y.A. Wu, L. Li, Z. Li, A. Kinaci, M.K. Chan, Y. Sun, J.R. Guest, I. Mcnulty, T. Rajh, Y. Liu, ACS Nano **10**, 3738 (2016)
23. Y. Xie, Y. Dai, X. Yuan, L. Jiang, L. Zhou, Z. Wu, J. Zhang, H. Wang, T. Xiong, J. Colloid Interface Sci. **530** (2018)
24. L. Ju, P. Wu, Q. Yang, Z. Ahmed, N. Zhu, Appl. Catal. B Environ. **224**, 159 (2018)
25. J. Yu, G. Dai, B. Huang, J. Phys. Chem. C **113**, 16394 (2009)
26. Y. Xu, H. Xu, H. Li, J. Xia, C. Liu, L. Liu, J. Alloys Compd. **509**, 3286 (2011)
27. Y. Chen, G. Zhu, Y. Liu, J. Gao, C. Wang, R. Zhu, P. Liu, J. Mater. Sci. Mater. Electron. **28**, 2859 (2017)
28. Y. Liang, S. Lin, L. Li, J. Hu, W. Cui, Appl. Catal. B **164**, 192 (2015)
29. Z. Lou, B. Huang, Z. Wang, X. Ma, R. Zhang, X. Zhang, X. Qin, Y. Dai, M.H. Whangbo, ChemInform **45**, 3873 (2015)
30. J. Qin, N. Chen, C. Feng, H. Chen, M. Li, Y. Gao, Catal. Lett. **148**, 2777 (2018)
31. H. Chen, N. Chen, C. Feng, Y. Gao, J. Colloid Interface Sci. **515**, 119 (2018)
32. M. Zhu, P. Chen, M. Liu, J. Mater. Chem. **22**, 21487 (2012)
33. B. Golzad-Nonakaran, A. Habibi-Yangjeh, Adv. Powder Technol. **27**, 1427 (2016)
34. I.P. Sahu, D.P. Bisen, N. Brahme, Phys. Procedia **76**, 80 (2015)
35. S.F. Yang, C.G. Niu, D.W. Huang, H. Zhang, G.M. Zeng, J. Colloid Interface Sci. **505**, 96 (2017)
36. Y. Liang, S. Lin, L. Liu, J. Hu, W. Cui, Appl. Catal. B **164**, 192 (2015)
37. Y. Wang, C.G. Niu, L. Wang, Y. Wang, X.G. Zhang, G.M. Zeng, RSC Adv. **6**, 47873 (2016)
38. X. Li, S. Fang, G. Lei, C. Han, Q. Ping, W. Liu, Appl. Catal. B Environ. **s176–177**, 62 (2015)
39. S. Jafari, A. Nezamzadeh-Ejhieh, J. Colloid Interface Sci. **490**, 478 (2017)
40. Y. Gong, X. Quan, H. Yu, S. Chen, Appl. Catal. B **219**, 439 (2017)
41. J. Wang, Y. Yu, L. Zhang, Appl. Catal. B **136–137**, 112 (2013)
42. P. Raizada, P. Singh, A. Kumar, G. Sharma, B. Pare, S.B. Jonnalagadda, P. Thakur, Appl. Catal. A **486**, 159 (2014)
43. P. Shandilya, D. Mittal, M. Soni, P. Raizada, A. Hosseini-Bandegharaei, A.K. Saini, P. Singh, J. Clean. Prod. **203**, 386 (2018)
44. P. Shandilya, D. Mittal, A. Sudhaik, M. Soni, P. Raizada, A.K. Saini, P. Singh, Sep. Purif. Technol. **210**, 804 (2019)
45. P. Shandilya, D. Mittal, M. Soni, P. Raizada, J.-H. Lim, D.Y. Jeong, R.P. Dewedi, A.K. Saini, P. Singh, J. Taiwan Inst. Chem. Eng. **93**, 528 (2018)
46. Y. Zhang, L. Wang, X. Kong, H. Jiang, F. Zhang, J. Shi, J. Colloid Interface Sci. **522**, 29 (2018)
47. J. Qin, N. Chen, C. Feng, H. Chen, Z. Feng, Y. Gao, Z. Zhang, Catal. Lett. **149**, 891 (2019)
48. L. Jing, Y. Xu, S. Huang, M. Xie, M. He, H. Xu, H. Li, Q. Zhang, Appl. Catal. B **199**, 11 (2016)
49. Y. Yang, Y. Guo, F. Liu, X. Yuan, Y. Guo, S. Zhang, W. Guo, M. Huo, Appl. Catal. B **142–143**, 828 (2013)
50. M. Xu, L. Han, S. Dong, ACS Appl. Mater. Interfaces **5**, 12533 (2013)